International Journal of Technology 15(5) 1292-1307 (2024)
Received November 2023 / Revised March 2024 / Accepted April 2024

International Journal of Technology

http://ijtech.eng.ui.ac.id

Modeling Dynamic Recrystallization Kinetics in BS 080M46 Medium Carbon Steel: Experimental Verification and Finite Element Simulation

Nattarawee Siripath[1], Surasak Suranuntchai[1*], Sedthawatt Sucharitpwatskul[2]

[1]*Department of Tool and Materials Engineering, Faculty of Engineering, King Mongkut's University of Technology, Thonburi, Bangkok, 10140, Thailand*
[2]*National Science and Technology Development Agency (NSTDA), Thailand Science Park, Phahonyothin Road, Khlong Nueng, Khlong Luang, Pathum Thani, 12120, Thailand*

Abstract. Utilized the experimental data to construct models that describe DRX kinetics and the evolution of grain size, employing the Johnson-Mehl-Avrami-Kolmogorov (JMAK) equation, this study investigates the dynamic recrystallization (DRX) characteristics and the microstructure evolution within BS 080M46 medium carbon steel under high-temperature conditions. Several trials were carried out to analyze hot compression, covering a temperature range of 900°C to 1200°C and utilizing varying strain rates of 0.1, 1, and 10 s-1. The incorporation of these models into QForm V10.2.1 facilitated finite element modeling (FEM) simulation, enabling the evaluation of DRX behavior. A comparative analysis was carried out to confirm the efficacy of the developed models, aligning the simulation results with the data obtained through metallographic observations. The high level of agreement between the simulation and experimental findings related to the DRX grain size was quantified by a correlation coefficient (R) of 0.991, along with an average absolute relative error (AARE) of 7.412%. These results confirm the capability of the developed DRX kinetics and grain size evolution models in accurately predicting the grain size of BS 080M46 medium carbon steel. In addition, the study suggests that higher temperatures or lower strain rates can result in an increased volume fraction of dynamic recrystallization (DRX) and grain size. This highlights the importance of Finite Element Method (FEM) as a crucial tool for comprehending the evolution of microstructure during hot working processes.

Keywords: BS 080M46 medium carbon steel; DRX behavior; Finite element modeling; Grain size; Hot compression test

1. Introduction

BS 080M46 is a versatile medium carbon steel known for its excellent mechanical properties and ease of processing, making it ideal for high-stress applications requiring wear resistance. Its strength, toughness, and wear resistance have led to its widespread use in various machinery parts such as gears, axles, crankshafts, and connecting rods, as well as in shafts, bolts, studs, and hydraulic cylinders (Mizuguchi *et al.,* 2009). Typically, during the hot working process of BS 080M46 medium carbon steel, the material is heated to a temperature exceeding the recrystallization temperature range. This allows for the material to be plastically shaped and formed easily using various hot working processes, including hot forging, hot rolling, and hot extrusion (Altan, 2005). Lv *et al.* (2018)

*Corresponding author's email: surasak.sur@kmutt.ac.th, Tel.: +66-2-4709213; Fax: +66-2-8729080
doi: 10.14716/ijtech.v15i5.6770

emphasized that thermo-mechanical processing, utilized in the production of large structural components, tailors the microstructure for desired mechanical properties, necessitating predictive models due to the sensitivity of the microstructure to processing conditions, and the intricate relationship between processing parameters, material deformation behavior, and resulting microstructures.

In the realm of metallurgy, three significant phenomena – work hardening (WH), dynamic recovery (DRV), and dynamic recrystallization (DRX) – significantly shape the flow behavior, microstructure, and energy required during the hot working process, occurring concurrently during material deformation and controlling flow stress under varying conditions (Derazkola *et al.*, 2022; Kooiker, Perdahcıoğlu, and Boogaard, 2018). These phenomena ultimately impact material properties and behavior, playing a critical role in determining the quality of the final product (Chen *et al.*, 2021b). Through these occurrences, the microstructure evolution of metals is notably influenced by DRX. The existing coarse grains undergo notable deformation and eventually transform into smaller, equiaxed grains, contributing to both grain refinement and homogenization (Bharath *et al.*, 2021; Zheng *et al.*, 2018; Quan, 2013). Consequently, this process leads to enhanced mechanical properties, particularly in terms of increased strength, ductility, and toughness (Tukiat *et al.*, 2024; Zou *et al.*, 2022; Anwar *et al.*, 2021; Kurnia and Sofyan, 2017; Kozmel *et al.*, 2014). The effects of DRX on metals depend on several factors, including the composition of the metal, the deformation temperature, the strain rate, and the processing history (Alaneme and Okotete, 2019). In addition, the occurrence of DRX and the resulting microstructure can also be affected by prior cold work, which may require higher processing temperatures or longer processing times to achieve DRX (Stefani *et al.,* 2016; Sanrutsadakorn, Uthaisangsuk, and Suranuntchai, 2014).

Precisely characterizing the DRX behaviors and the mechanisms of grain evolution is of utmost importance for achieving the desired microstructure and mechanical properties. The construction of DRX kinetic models has involved several attempts to represent material behavior and the evolution of grain size effectively. Studies by Hu and Wang (2020) and Yang *et al.* (2018) have shown that flow curves can represent the hot working behaviors of BT25y titanium alloy and 5CrNiMoV steel, respectively, due to their close correlation with microstructural changes. Therefore, stress-strain data derived from isothermal compressions can be employed to formulate DRX kinetics, with the Johnson-Mehl-Avrami-Kolmogorov (JMAK) equation widely utilized to depict the correlation between the volume fraction of deformation-induced DRX, deformation temperature, and strain rate (Irani *et al.,* 2019). For instance, Wang *et al.* (2016), through their research, established an Arrhenius-type constitutive equation incorporating a Zener-Hollomon parameter, along with DRX volume fraction and grain size models, all based on the JMAK equation. This comprehensive approach accurately describes the deformation behavior observed during the hot-working processes of the carburizing steel alloy 20Cr2Ni4A. Similarly, models for the DRX volume fraction and grain size, applicable to 33Cr23Ni8Mn3N heat-resistant steel, were developed by Ji *et al.* (2020) and integrated these models into the DEFORM-3D software. The finding stemming from microstructural observations obtained through LOM and SEM, along with finite element simulations, exhibited highly consistent, thereby validating the precision of the established DRX model. Quan *et al.* (2019) investigated the DRX behavior of AlCu4SiMg alloys using the JMAK equation and verified its feasibility through both FE simulations and experiments. Additionally, studies on various alloys such as Ti-5Al-5Mo-5V-3Cr-1Zr near b Titanium alloy (Lv *et al.*, 2018), medium Mn steel (Sun *et al.*, 2020), solution-treated Ni-based superalloy (Chen *et al.*, 2016), Cr8 alloy (Chen *et al.*, 2022), and TB8 Titanium alloys (Zhang *et al.*, 2020) used FEM simulations of DRX behavior. The concordance between simulation results and microstructural observations underscores the potential of finite element

simulations as valuable tools for predicting the DRX behavior across various alloys, which can be helpful in designing and optimizing manufacturing processes for these materials.

Despite extensive research into understanding dynamic recrystallization (DRX) phenomena in various alloys, the specific behavior of DRX in BS 080M46 medium carbon steel remains relatively unexplored. This knowledge gap presents significant challenges in optimizing the hot working processes of this material to achieve the desired microstructural characteristics and mechanical properties. Furthermore, the lack of accurate predictive models tailored to BS 080M46 medium carbon steel further hinders process optimization efforts. Therefore, the present work aims to address these challenges by studying the DRX behavior and microstructure evolution of BS 080M46 medium carbon steel through hot compression testing. Experimental data were collected to establish both a DRX kinetics model and a grain size model based on the JMAK equation. These models were subsequently incorporated into QForm V10.2.1 software to simulate microstructure evolution, with a specific emphasis on grain size under different deformation conditions. By comparing these finite element simulation results with microstructure observations, the accuracy and reliability of the models are verified. Providing insights into DRX behavior specific to BS 080M46 medium carbon steel and developing accurate predictive models, this study aims to contribute to the advancement of metallurgical science and materials engineering, facilitating enhanced process optimization and product development in engineering applications.

2. Methodology

The material being studied is BS 080M46 medium carbon steel, which was supplied by S.B.-CERA Co., Ltd. The weight percentage (wt%) of the steel's chemical composition was analyzed using an Emission Spectrometer (OES) and is detailed in Table 1. Figure 1(a) illustrates the conceptual methodology diagram used in this study. The flow curves under high temperatures required for input into the finite element model were obtained by a hot compression test using a Baehr DIL-805 deformation dilatometer. Samples were prepared in a cylindrical shape, 5 mm in diameter and 10 mm in height, with a thermocouple attached to the surface for direct temperature detection during deformation. The hot compression test covered four temperatures: 900°C, 1000°C, 1100°C, and 1200°C, along with three strain rates: 0.1, 1, and 10 s^{-1}, to characterize deformation conditions. Samples were placed in a vacuum chamber filled with inert Argon gas and heated by an induction coil to reach the deformation temperatures. The heating rate of 1.625°C/s was maintained for 1 minute to ensure uniform temperature distribution. Samples were then compressed using an Alumina punch to achieve a 60% reduction in height, followed by immediate quenching in Argon gas with a cooling rate of 40°C/s until reaching room temperature. Figure 1(b) depicts the temperature–time path during the hot compression test. Metallographic preparation involved cutting samples along the cylindrical axis, mounting them on a hot press, initial polishing with 400-grit SiC abrasive paper, followed by finer grits up to 1200 grit SiC papers and 0.3 μm Alumina particles for final polishing. Subsequently, surfaces were etched using a 4% picral and 3% Nital solution for 4 seconds. Microstructural observations were conducted using Light Optical Microscopy (LOM) and scanning electron microscopy (SEM), focusing on the central region of the sample's cross-sections. The initial microstructure of BS 080M46 medium carbon steel contains proeutectoid ferrite and pearlite, as depicted in Figure 2.

Table 1 Chemical compositions (wt%) of BS 080M46 medium carbon steel

C	Si	Mn	P	S	Ni	Cr	Mo	Cu
0.467	0.194	0.673	0.027	0.021	0.068	0.110	0.016	0.178

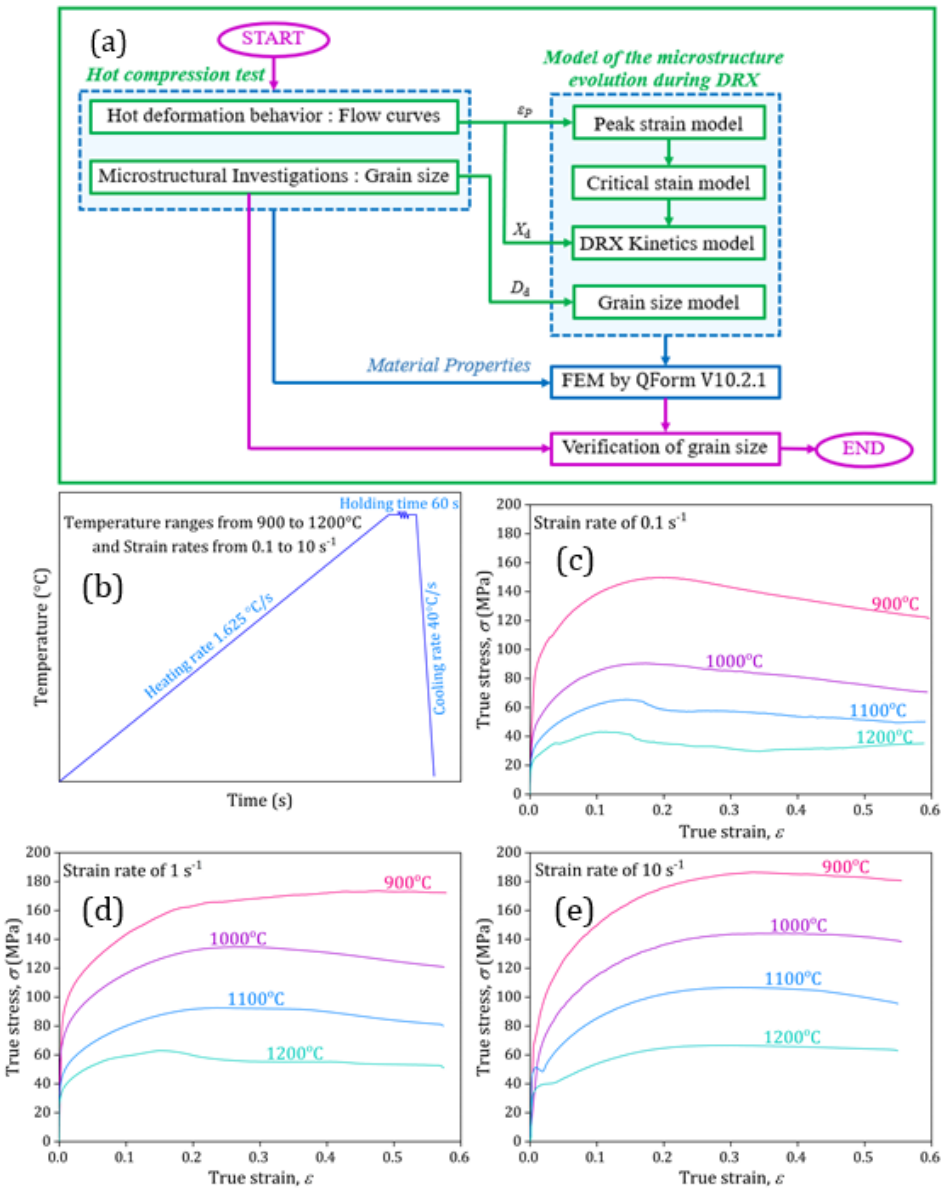

Figure 1 (a) Methodology concept diagram; (b) Experimental hot compression test deformation route of the hot compression test and flow curves of BS 080M46 steel at the strain rate of (c) 0.1 s^{-1}; (d) 1 s^{-1}; and (e) 10 s^{-1} with varying deformation temperature

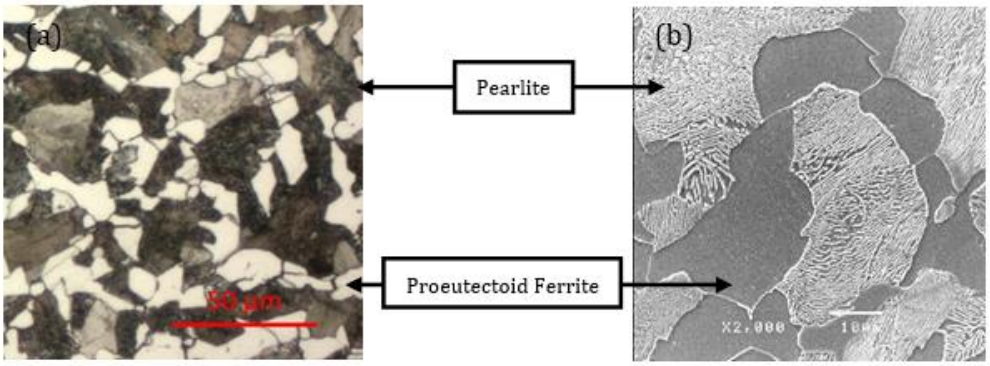

Figure 2 Microstructure of BS 080M46 medium carbon steel by (a) LOM and (b) SEM showing proeutectoid ferrite and pearlite structure

3. Results and Discussion

3.1. Flow curve of BS 080M46 medium carbon steel

The collected experimental data is employed to generate flow curves of BS 080M46 medium carbon steel, systematically plotted over a range of deformation temperatures spanning from 900 to 1200°C at 100°C intervals with constant strain rates of 0.1, 1, and 10 s^{-1}, as illustrated in Figure 1(c) to Figure 1(e). Flow curves represent the stress-strain relationship under well-defined deformation conditions. They often exhibit a characteristic behavior known as dynamic recrystallization (DRX), which starts with a peak stress and gradually declines towards a state of steady stress, as highlighted in Mirzadeh *et al.* (2012) and (Mirzadeh, 2015).

In the beginning, stress starts to rise as the strain continuously increases, which is governed by work hardening. The dislocations within the material move and accumulate at the grain boundaries, leading to deformation resistance and strengthening. This phenomenon is commonly referred to as work hardening, which makes the material stronger and more resistant to deformation. At this point, the strain has not yet reached its critical value. As dislocations accumulate and undergo rearrangement, sub-boundaries are formed. These sub-boundaries play a role in triggering the onset of DRX. DRX begins when the strain exceeds a critical value, resulting in the softening mechanism, meaning the material becomes more pliable and transforms from a previously strengthened state. This rapid transformation gradually converts the accumulated energy at the grain boundaries due to the work hardening process into activation energy for DRX, facilitating the formation and growth of equiaxed grains and inducing a change in the microstructure of the material. Nevertheless, with the increasing strain, the dislocation density rises, and the softening effect tends to gradually become higher. Consequently, the flow stress rises while the increasing rate slightly continuously decreases. At the point of balance between work hardening and softening mechanisms, driven by DRX, the stress reaches its peak, and then exhibits a slight decline until it reaches steady-state stress.

3.2. Establishment of DRX model of BS 080M46 medium carbon steel

3.2.1. Determination of Critical Strain Model Parameters

During the hot working process, the initial stage of compressive deformation shows a rapid rise to a peak in the experimental flow curves with an increase in true strain. This is subsequently followed by a gradual reduction, ultimately leading to a consistent, steady-state stress. The strain value associated with the peak stress (σ_p) is commonly denoted as the peak strain (ε_p).

The initiation of DRX is typically correlated with the dislocation accumulation, which may arise due to plastic deformation. DRX can be initiated when the dislocation density exceeds a certain critical point, commonly termed the critical strain (ε_c) for DRX (Wu *et al.*, 2018). New grains can nucleate both at the pre-existing grain boundaries and within the grains that have undergone deformation, and these newly generated grains can grow into high-angle boundaries. The work hardening rate, denoted as θ (MPa), is expressed as the derivative of $d\sigma/d\varepsilon$ (Chen *et al.*, 2021a; Shafiei and Ebrahimi, 2012; Najafizadeh and Jonas, 2006). In their findings, Poliak and Jonas (2003) proposed that the inflection observed in $\ln\theta - \varepsilon$ plots can serve as a valuable indicator for identifying the initiation of DRX. The $\ln\theta - \varepsilon$ analysis was effective in providing precise values for determining critical strain (Mirzadeh and Najafizadeh, 2010a; 2010b). Applying a third-order polynomial regression method to analyze the curve until it reaches its peak facilitates the identification of the inflection point, thereby allowing for the derivation of the critical strain (ε_c) corresponding to the critical stress (σ_c). Figure 3(a) displays the $\ln\theta - \varepsilon$ curves and their associated 3rd-order polynomial

for a strain rate of 0.1 s^{-1}. The presented data in Table 2 exhibits the values for ε_p and ε_c under various deformation conditions. These values have been computed from the experimental stress-strain curves and work hardening rate curves. According to Figure 3(b), the normalized strain can is represented by the ratio $\varepsilon_c/\varepsilon_p$, with a value of 0.478

Table 2 Values of ε_p, ε_c, $\varepsilon_{0.5}$ and D_d for BS 080M46 medium carbon steel

$\dot{\varepsilon}$ (s^{-1})	T (°C)	ε_p	ε_c	$\varepsilon_{0.5}$	D_d (μm)
0.1	900	0.194	0.093	0.400	7.08
	1000	0.174	0.083	0.388	11.09
	1100	0.146	0.070	0.280	16.74
	1200	0.106	0.051	0.160	32.76
1	900	0.478	0.230	0.467	6.35
	1000	0.282	0.136	0.452	9.65
	1100	0.236	0.113	0.463	13.46
	1200	0.152	0.074	0.303	30.37
10	900	0.336	0.159	0.526	5.51
	1000	0.384	0.182	0.509	8.29
	1100	0.316	0.150	0.485	12.21
	1200	0.292	0.139	0.464	20.12

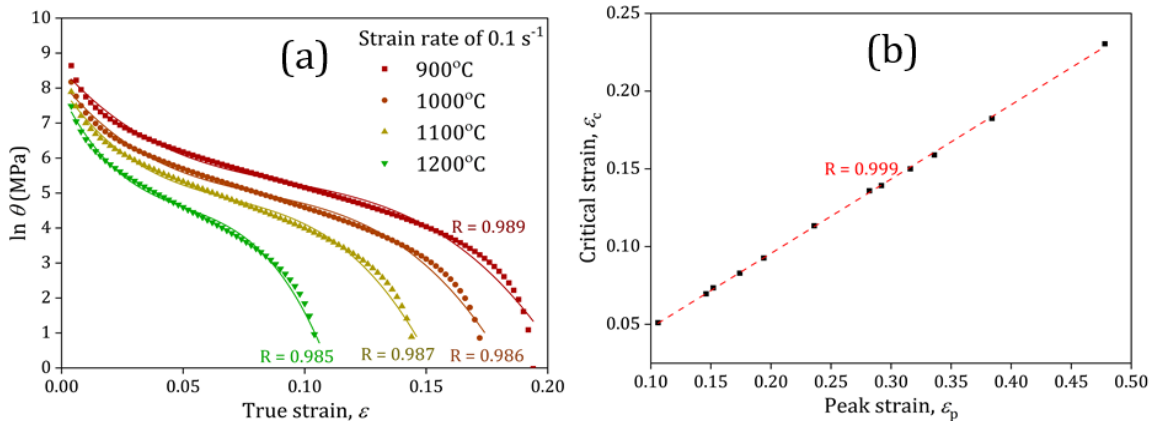

Figure 3 (a) $\ln\theta - \varepsilon$ curve of BS 080M46 medium carbon steel and their corresponding 3rd order polynomial at a strain rate of 0.1 s^{-1} and (b) ε_c versus ε_p

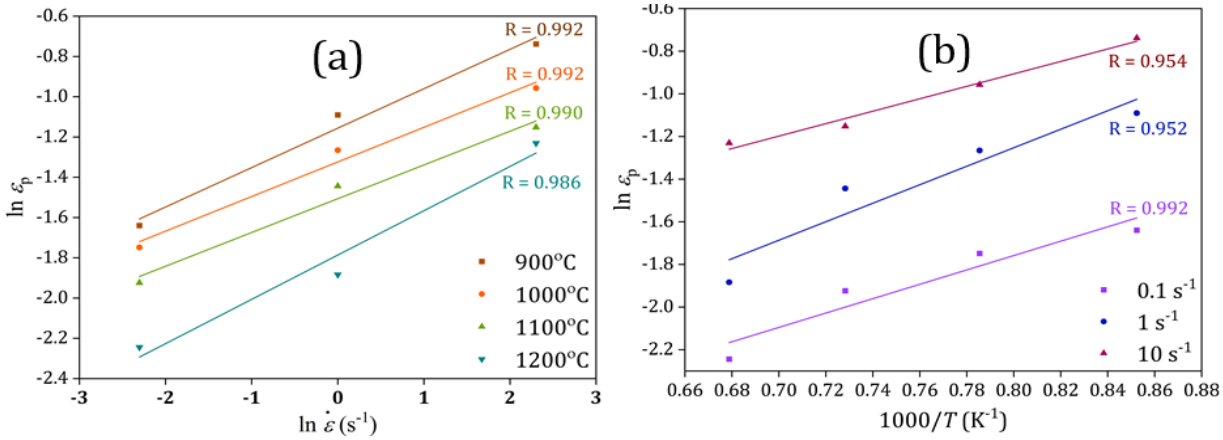

Figure 4 Scatter plot and their linear regression of (a) $\ln\varepsilon_p - \ln\dot{\varepsilon}$ and (b) $\ln\varepsilon_p - 1000/T$

Taking into consideration the initial grain size (d_0), temperature (T), strain rate ($\dot{\varepsilon}$), and the activation energy for deformation (Q), one can formulate the expression for ε_p as follows (Chen *et al.*, 2022; Wang *et al.*, 2011):

$$\varepsilon_{\mathrm{p}} = A_{\mathrm{p}} d_0^{M_{\mathrm{p}}} \dot{\varepsilon}^{L_{\mathrm{p}}} \exp\left(\frac{Q_{\mathrm{p}}}{RT}\right) \quad (1)$$

where the constants A_{p}, M_{p}, and L_{p} are associated with the material. With a value of 8.314 J·K^{-1}mol^{-1}, R represents the universal gas constant. All deformed samples share the same initial grain size. However, the influence of grain size is subsequently taken into consideration, resulting in $M_{\mathrm{p}} = 0$. Obtaining the values of A_{p}, L_{p}, and Q_{p} involves applying the natural logarithm for both sides of Equation 1, yielding in Equation 2, as depicted below:

$$\ln \varepsilon_{\mathrm{p}} = \ln A_{\mathrm{p}} + L_{\mathrm{p}} \ln \dot{\varepsilon} + \frac{Q_{\mathrm{p}}}{RT} \quad (2)$$

The material constant L_{p} is provided at a certain temperature $L_{\mathrm{p}} = \partial \ln \varepsilon_{\mathrm{p}} / \partial \ln \dot{\varepsilon}$. The fitted linear correlation with temperature variations between $\ln \varepsilon_{\mathrm{p}}$ and $\ln \dot{\varepsilon}$ is depicted in Figure 4(a). Consistent slopes across a range of temperatures result in L_{p} being computed as 0.189, obtained by averaging the slopes of the four fitted curves. In accordance with the correlation between $\ln \varepsilon_{\mathrm{p}}$ and $1000/T$ under varying strain rates, Q_{p} can be calculated at a certain strain rate $Q_{\mathrm{p}} = R\partial \ln \varepsilon_{\mathrm{p}} / \partial T^{-1}$. The Q_{p} could be obtained by linear fitting the data in Figure 4(b), and the average of the four slope values for Q_{p} was found to be 29448.7 J·mol^{-1}. The value of A_{p} was also computed as 0.012 by substituting the average of L_{p} and Q_{p} into Equation 1. Hence, Equation 3 can be given as:

$$\varepsilon_{\mathrm{p}} = 0.012 \dot{\varepsilon}^{0.189} \exp\left(\frac{29448.7}{RT}\right) \quad (3)$$

The critical strain model was $\varepsilon_{\mathrm{c}} = \alpha \varepsilon_{\mathrm{p}} = 0.478 \varepsilon_{\mathrm{p}}$

$$\varepsilon_{\mathrm{c}} = 0.006 \dot{\varepsilon}^{0.189} \exp\left(\frac{29448.7}{RT}\right) \quad (4)$$

3.2.2. Determination of DRX Kinetics Model Parameters

Through the utilization of stress-strain data from the experiment, cited in references (Joun *et al*., 2022; Jantepa and Suranuntchai, 2021; Lv *et al*., 2018) one can directly compute the DRX volume fraction (X_{d}) with the aid of Equation 5.

$$X_{\mathrm{d}} = (\sigma_{\mathrm{p}} - \sigma)/(\sigma_{\mathrm{p}} - \sigma_{\mathrm{ss}});\ (\varepsilon \geq \varepsilon_{\mathrm{c}}) \quad (5)$$

where σ_{p} denotes the peak stress, and σ_{ss} represents the steady-state stress. The DRX kinetics model, based on the JMAK equation in alloys, has been widely adopted due to the findings of several studies (Zhang *et al*., 2022a; Joun *et al*., 2022; Ji *et al*., 2021; 2020; Sun *et al*., 2020; Zhang *et al*., 2020; 2019; Marques Ivaniski *et al*., 2019; Quan *et al*., 2019; Wang *et al*., 2016). At elevated temperatures, Equation 6 serves as a tool to observe the evolution of the DRX volume fraction.

$$X_{\mathrm{d}} = 1 - \exp\left[-\beta_{\mathrm{d}} \left(\frac{\varepsilon - \varepsilon_{\mathrm{c}}}{\varepsilon_{0.5}}\right)^{k_{\mathrm{d}}}\right] \quad (6)$$

In QForm software, the DRX volume fraction is expressed as:

$$X_{\mathrm{d}} = 1 - \exp\left[-\beta_{\mathrm{d}} \left(\frac{\varepsilon - \varepsilon_{\mathrm{c}}}{A_{0.5} d_0^{M_{0.5}} \dot{\varepsilon}^{L_{0.5}} \exp(Q_{0.5}/RT)}\right)^{k_{\mathrm{d}}}\right] \quad (7)$$

This equation, referred to as Equation 7, describes the evolution of the DRX volume fraction as a function of strain. Furthermore, the strain required to achieve a 50% DRX volume fraction, as calculated using Equation 8, can be determined based on the existing literature.

$$\varepsilon_{0.5} = A_{0.5} d_0^{M_{0.5}} \dot{\varepsilon}^{L_{0.5}} \exp\left(\frac{Q_{0.5}}{RT}\right) \quad (8)$$

where $A_{0.5}$, $M_{0.5}$, and $L_{0.5}$ represent material constants, while $Q_{0.5}$ denotes the activation energy related to recrystallization. Additionally, β_d and k_d are the material-specific constants in the JMAK equation. The initial grain size was not taken into account due to the observation that the average grain size of one specimen was found to be the same as that of the others, resulting in $M_{0.5}$ = 0. Achieving Equation 9 involves the application of the natural logarithm to Equation 8 on both sides.

$$\ln \varepsilon_{0.5} = \ln A_{0.5} + L_{0.5} \ln \dot{\varepsilon} + \frac{Q_{0.5}}{RT} \tag{9}$$

Equation 9 yield $L_{0.5} = \partial \ln \varepsilon_{0.5} / \partial \ln \dot{\varepsilon}$ and $Q_{0.5} = R\partial \ln \varepsilon_{0.5} / \partial T^{-1}$. Additionally, Equation 5 allows the calculation of the stress at which 50% of the DRX volume fraction occurs. The associated strain, $\varepsilon_{0.5}$, can be calculated based on the experimental stress-strain data provided in Table 2. The plots representing $\ln \varepsilon_{0.5} - ln\dot{\varepsilon}$ and $\ln \varepsilon_{0.5} - 1000/T$ can be illustrated in Figure 5(a) and Figure 5(b), respectively. Subsequent to the application of linear regression fitting, the computed average material constants are as follows: $L_{0.5}$ = 0.117 and $Q_{0.5}$ = 22058.4 J·mol^{-1}. By substituting $L_{0.5}$ and $Q_{0.5}$ into Equation 8, the average value of $A_{0.5}$ from twelve deformation conditions is 0.040. Equation 10 can be given as:

$$\varepsilon_{0.5} = 0.040\dot{\varepsilon}^{0.117} \exp\left(\frac{22058.4}{RT}\right) \tag{10}$$

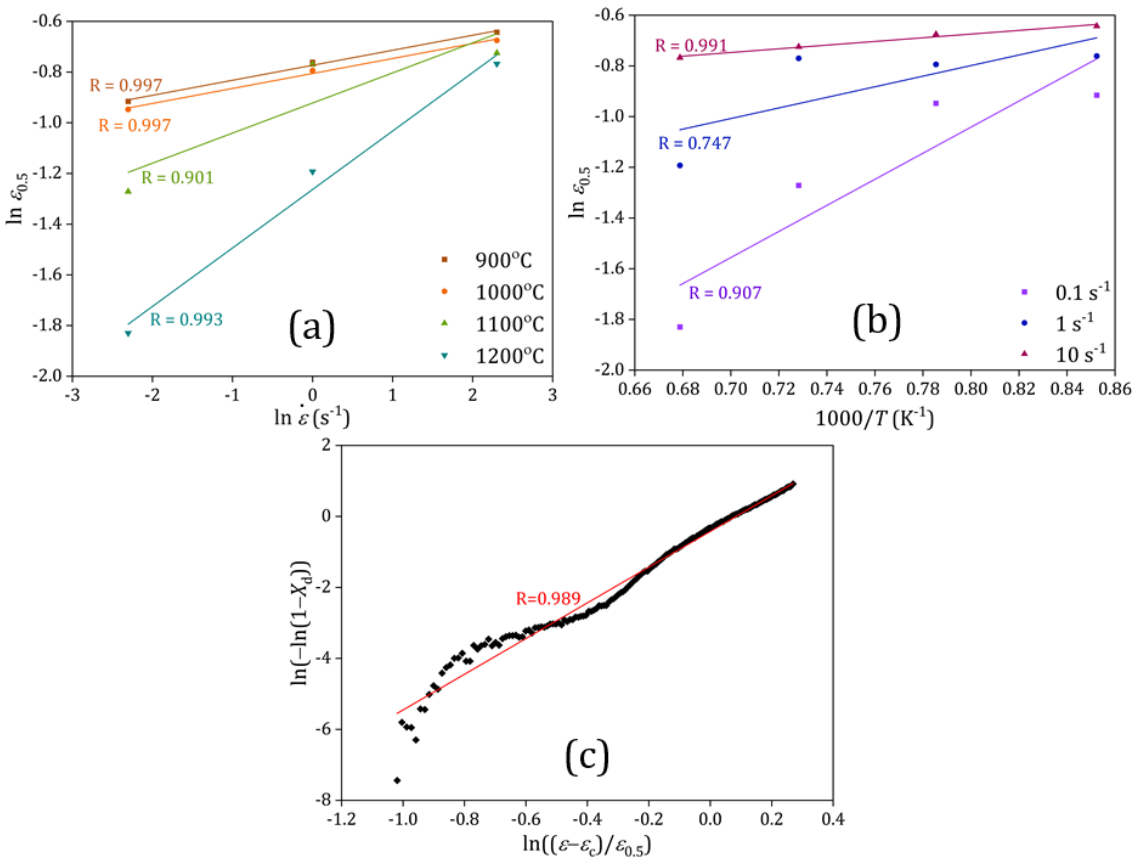

Figure 5 Scatter plot and their linear regression of (a) $\ln \varepsilon_{0.5} - ln\dot{\varepsilon}$ and, (b) $\ln \varepsilon_{0.5} - 1000/T$ and (c) correlation of $\ln(-\ln(1 - X_d))$ and $\ln((\varepsilon - \varepsilon_c)/\varepsilon_{0.5})$ at 1100°C under a strain rate of 1 s^{-1}

Upon performing the natural logarithm on both sides of Equation 10, the values of k_d and β_d, are obtained, as shown:

$$\ln(-\ln(1 - X_d)) = \ln \beta_d + k_d \ln\left(\frac{\varepsilon - \varepsilon_c}{\varepsilon_{0.5}}\right) \tag{11}$$

Under the conditions of 1100°C and a strain rate of 1 s^{-1}, the relationship between $\ln(-\ln(1-X_d))$and $\ln((\varepsilon-\varepsilon_c)/\varepsilon_{0.5})$ exhibited a nearly linear trend, as shown in Figure 5(c). Here k_d corresponds to the slope of the regression line and ln β_d indicates the regression intercept. The average calculated values for k_d and β_d are 5.070 and 2.404, respectively. Ultimately, the DRX kinetic model of BS 080M46 medium carbon steel can be written as follows:

$$X_d = 1 - \exp\left[-2.404\left(\frac{\varepsilon-\varepsilon_c}{\varepsilon_{0.5}}\right)^{5.070}\right] \quad (12)$$

Considering Equation 12, Figure 6(a) and Figure 6(b) present the X_d under a deformation temperature of 1000°C and a strain rate of 1 s^{-1}, respectively. According to the calculation from Equation 12, it becomes clear that an increase of the applied strain results in a proportional increase in the DRX volume fraction, ultimately nearing 1, or 100%. This observation strongly implies that the material undergoing deformation tends toward a complete DRX process. When applying a constant strain at a fixed strain rate of 1 s^{-1}, raising the deformation temperature accelerates the DRX phenomenon. The acceleration of this phenomenon arises from the increased mobility of grain boundaries in higher temperatures. This increased mobility promotes the initiation of new grains and facilitates the growth and merging of existing ones. This phenomenon enhances the nucleation and growth processes associated with DRX, ultimately leading to a higher DRX volume fraction. At a consistent deformation temperature of 1000°C, conversely, elevating the strain rate promotes grain boundary mobility. This increased mobility provides a longer duration for grain boundary migration, resulting in a delayed DRX. These findings suggest that the DRX volume fraction can be notably increased by elevating the deformation temperature and concurrently lowering the strain rate.

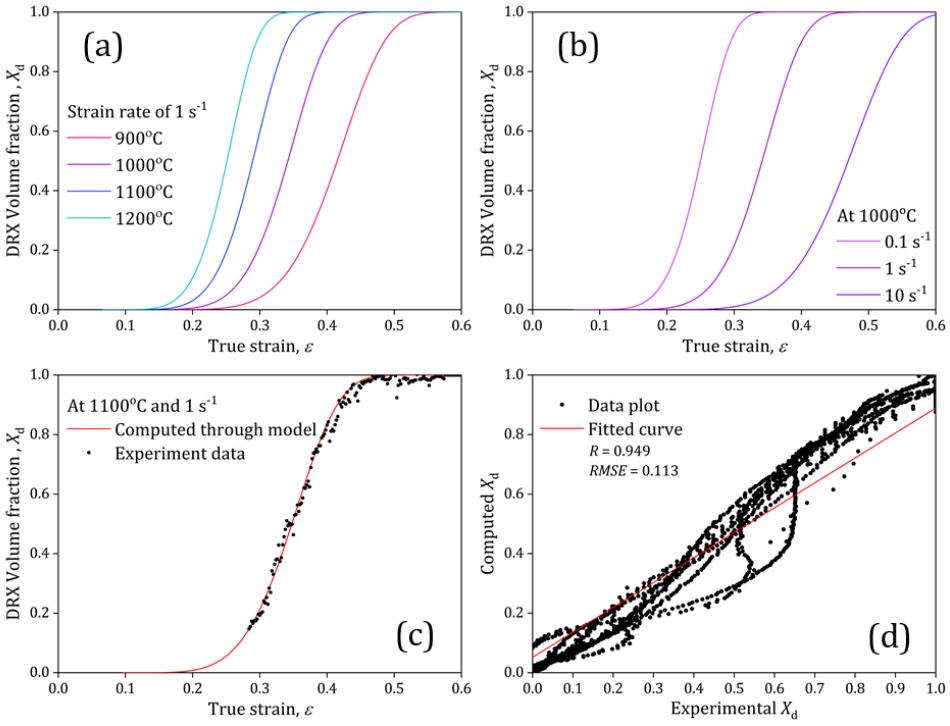

Figure 6 X_d versus ε curves at (a) 1 s^{-1} and (b) 1000 °C; (c) Comparing computed and experimental X_d values for a specific deformation condition; (d) Correlation between computed and experimental X_d values

The DRX kinetics model is applied to calculate the DRX volume fraction of BS 080M46 medium carbon steel within a range of deformation conditions. The plots in Figure 6(c) and Figure 6(d) illustrate the concordance between computed and experimental X_d values. In Figure 6(c), the comparison of the computed and experimental values of X_d is depicted for the hot compression test of BS 080M46 medium carbon steel under specific conditions (1100°C and a strain rate of 1 s^{-1}). Meanwhile, Figure 6(d) displays a scatter plot illustrating the correlation analysis between experimental and calculated DRX volume fraction values across all deformation conditions. The high correlation coefficient (R = 0.949) and low root mean square error ($RMSE$ = 0.113) confirm the accuracy and effectiveness of the DRX model in predicting X_d of BS 080M46 medium carbon steel during hot compression tests.

3.2.3. Determination of Grain size model parameters

The metallography method, in accordance with the ASTM E1382 standard, was employed to determine the average DRX grain size of BS 080M46 medium carbon steel. Figure 7 displays the optical microstructures of the specimens subjected to compression under different deformation conditions. The measured values obtained from the midpoint along the cross-section aligned with the compression axis are presented in Table 2. The average DRX grain size, as defined by Equation 13, is demonstrated in terms of both deformation temperature and strain rate.

$$D_d = A_d d_0^{M_d} \dot{\varepsilon}^{L_d} \exp\left(\frac{Q_d}{RT}\right) \quad (13)$$

where D_d is the average DRX grain size, A_d, M_d and L_d are material constants. The initial grain size was ignored, so M_d = 0. By analysing $\ln D_d - \ln \dot{\varepsilon}$ (Figure 8(a)) and $\ln D_d - 1000/T$ (Figure 8(b)) using linear regression, the values L_d = –0.073 and Q_d = –67793.2 J·mol^{-1} were determined. The A_d was calculated as 7082.57 by averages of substituting L_d and Q_d into Equation 13. The expression representing the model for calculating the average DRX grain size of BS 080M46 medium carbon steel is presented below:

$$D_d = 7082.57 \dot{\varepsilon}^{-0.073} \exp\left(\frac{-67793.2}{RT}\right) \quad (14)$$

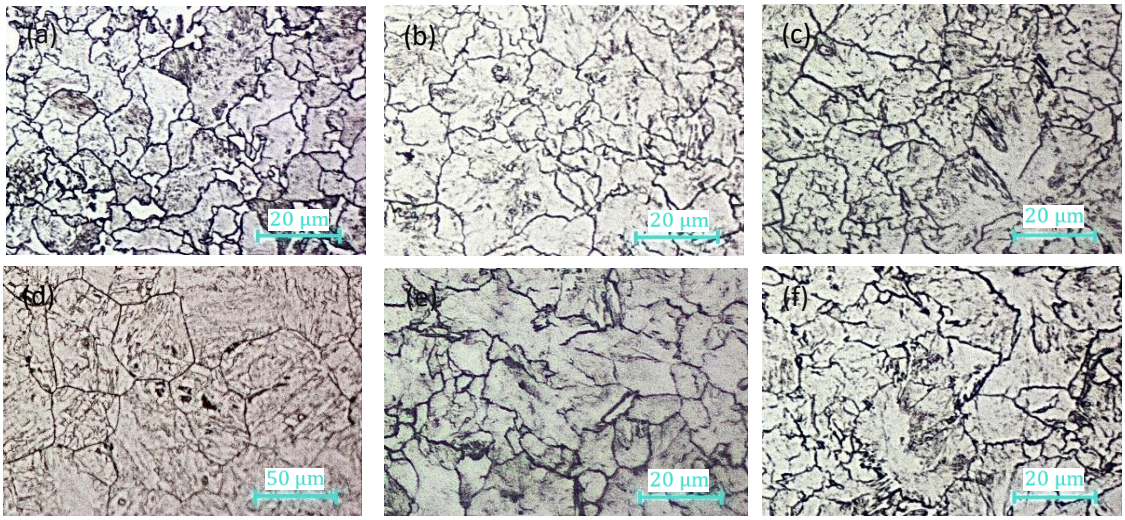

Figure 7 Optical microstructures of BS 080M46 medium carbon steel samples deformed at a strain of 0.6: (a) 900°C/1 s^{-1}, (b) 1000°C/1 s^{-1}, (c) 1100°C/1 s^{-1}, (d) 1200°C/1 s^{-1}, (e) 1100°C/1 s^{-1}, and (f) 1100°C/10 s^{-1}

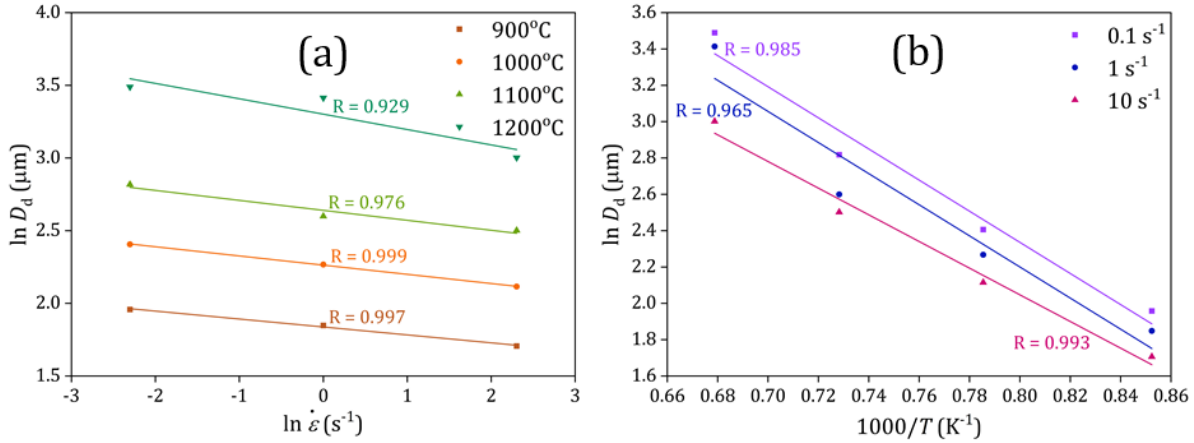

Figure 8 Relationship of (a) $\ln D_d - \ln \dot{\varepsilon}$ and (b) $\ln D_d - 1000/T$

3.3. FE Simulation of hot compression test

In evaluating the precision of both the DRX kinetics model and grain size model in the FE simulation of the hot compression test, the cylindrical billet with tetrahedral elements was employed, consisting of 139 nodes and 235 volumetric elements. The cylindrical billet was considered a deformable body, while the tools were defined as rigid bodies. Contact interfaces between the billet and tools adopt a shear type with a friction factor of 0.7. The processing conditions were set according to the experiment, with assumed uniform temperatures for samples, tools, and surroundings. Twelve sets of deformation conditions are selected to simulate the hot compression test. In order to shorten the computational time required for finite element simulation, a quarter of the cylindrical sample is used to simulate the hot compression test, based on the symmetry model. This approach is taken as an alternative to using the entire sample. The FE software for the simulation was QForm V10.2.1.

The FEM results are presented in contour color in Table 3, depicting the sample's deformation under a consistent strain rate of 1 s^{-1} across a range of temperatures of 900, 1000, 1100, and 1200°C. Additionally, Table 4 provides an overview of the effective strain, X_d, and D_d distribution obtained through FEM, while maintaining a constant deformation temperature of 1100°C and varying strain rates of 0.1, 1, and 10 s^{-1}, all corresponding to a strain value of 0.6. As seen in Table 3 and Table 4, for a given strain of 0.6 (reduction in height), the simulated results indicate that the lowest effective strain was observed precisely at the midpoint of the top and bottom regions of the cylindrical sample. Meanwhile the highest effective strain occurred at the midpoint along cross-section aligned with the compression axis, given deformation conditions. The processing parameters greatly influenced the effective strain. Due to the rise in temperature and the decrease in the strain rate, the deformed samples exhibited a more consistent distribution of strain at their center. During the deformation, the temperature of the billet is not uniform throughout the cross-section of the billet, resulting in thermal gradients. As a result, the center portion exhibited the maximum X_d value, where complete recrystallization is promoted, while the minimum value is located near the two end surfaces due to the thermal exchange between the tools and the external conditions, which can limit the extent of recrystallization and result in a lower DRX volume fraction. In addition, an elevated deformation temperature is associated with an expansion of the DRX zone. A higher strain rate results in a reduction in the complete DRX zone, and the incomplete DRX zone becomes larger. Regarding the grain size, an elevation in deformation temperature within the range of 900 to 1200°C induces a rise in the average grain size, going from 6.518 μm to 28.68. Conversely, when the strain rate is varied within a specific deformation temperature range from 0.1 to 10 s^{-1}, the average grain size decreases,

reducing from 14.5 μm to 12.15 μm. The simulation results were employed to determine the average grain size and subsequently compared with the grain size obtained through the analysis of images in metallography (Figure 7). The comparison is illustrated in the bar graph presented in Figure 9(a). In the evaluation of the accuracy and reliability of FEM results, this study incorporated commonly used standard statistical parameters (Zhang *et al.*, 2022a; Bharath *et al.*, 2021; Jantepa and Suranuntchai, 2021; Sun *et al.*, 2020; Zhang *et al.*, 2020), specifically, average absolute relative error (*AARE*) and the correlation coefficient (*R*).

Table 3 Distribution of effective strain, X_d, and D_d by FEM varying with a deformation temperature range of 900 to 1200°C at 1 s^{-1} for BS 080M46 medium carbon steel deformed at a strain of 0.6

T (°C)	900	1000	1100	1200
Effective strain	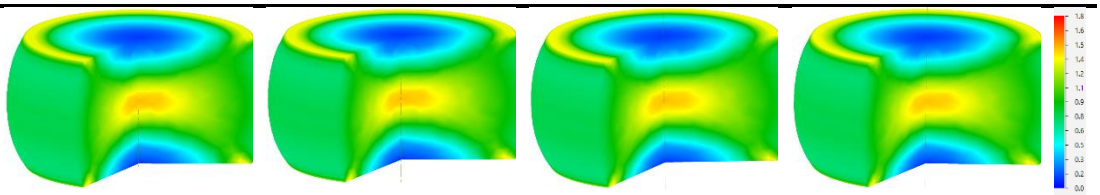			
DRX Volume fraction (X_d)	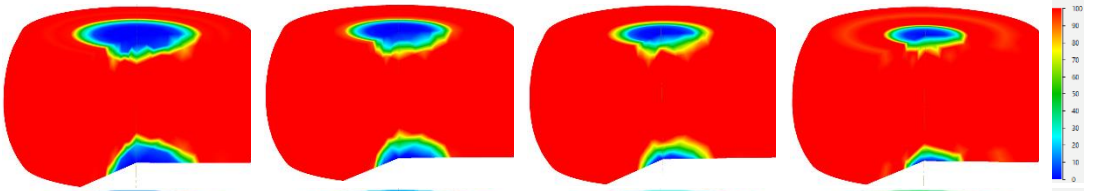			
Average grain size (D_d)	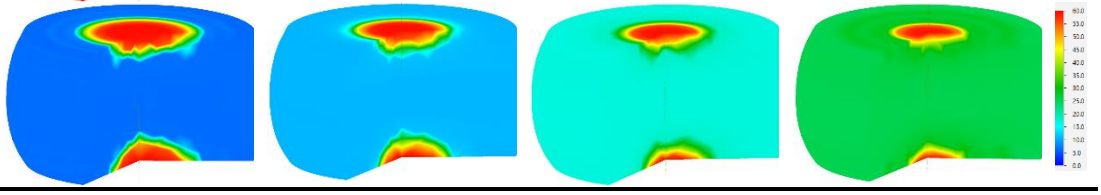			

Table 4 Distribution of effective strain, X_d, and D_d by FEM varying with strain rate range of 0.1 to 10 s^{-1} at 1100°C for BS 080M46 medium carbon steel deformed at a strain of 0.6

$\dot{\varepsilon}$ (s^{-1})	0.1	1	10
Effective strain	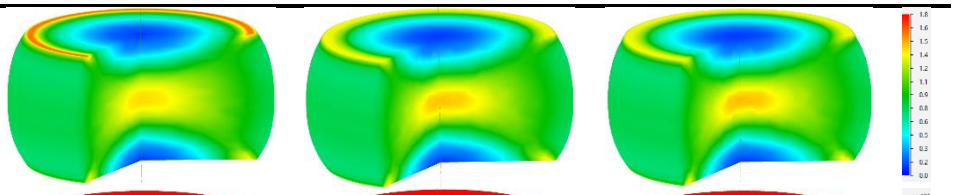		
DRX Volume fraction (X_d)	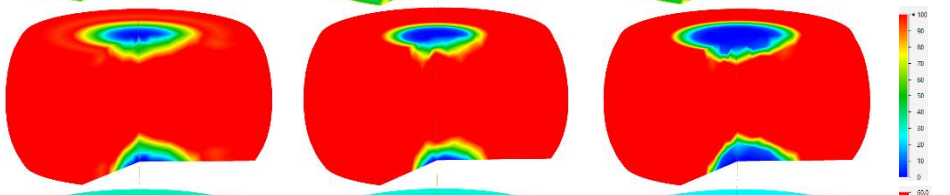		
Average grain size (D_d)	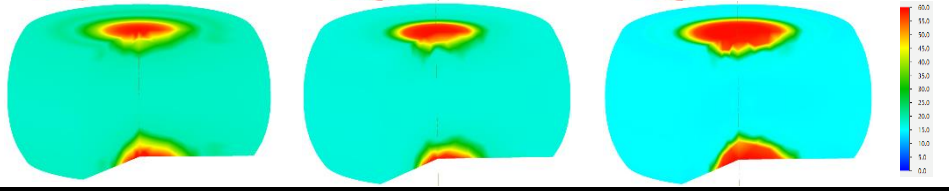		

In Figure 9(b), the graphical representation demonstrates a linear correlation between the average grain size from the FE simulation and the corresponding experimental data. By comparing the grain sizes obtained from the simulations and experiments conducted under

various deformation conditions, an *AARE* of 7.412% and an *R-value* of 0.991 were obtained. The strong alignment between the average grain size predicted via FE simulation and the experimental data highlights the effectiveness and reliability of the established grain size model in predicting the grain size of BS 080M46 medium carbon steel during hot working. The findings of this study exhibit conformity with the experimental observations and previously published results (Zhang *et al.*, 2022a; 2022b; Joun *et al.*, 2022; Ji *et al.*, 2021; 2020; Sun *et al.*, 2020; Zhang *et al.*, 2020; 2019; Marques Ivaniski *et al.*, 2019).

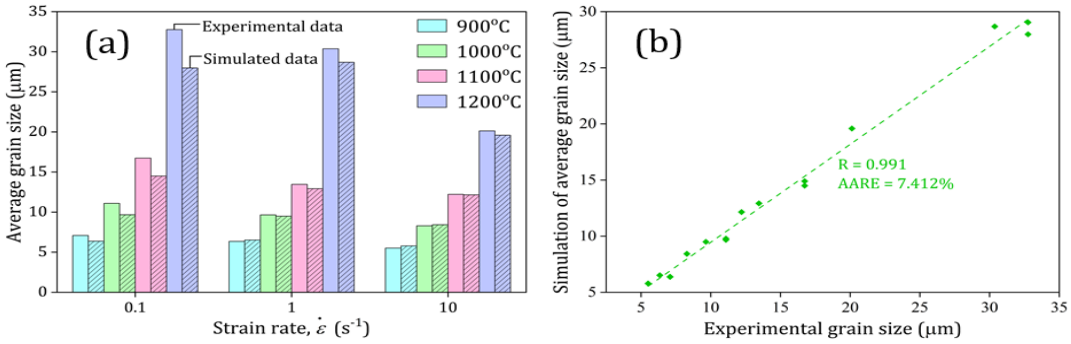

Figure 9 (a) Bar graph and (b) linear correlation between simulation and experimental D_d of BS 080M46 medium carbon steel under various deformations

4. Conclusions

In the present study, the dynamic recrystallization (DRX) characteristics and the microstructure evolution within BS 080M46 medium carbon steel under high-temperature conditions are investigated. Several trials were carried out to analyze hot compression, covering a temperature range of 900°C to 1200°C and utilizing varying strain rates of 0.1, 1, and 10 s^{-1}. The following conclusion have been obtained: The resulting flow curves depicted an initial peak stress followed by a gradual decline to a steady-state stress, underscoring the interplay between temperature and strain rate on flow stress; The critical strain, marking the onset of DRX, was observed from $\ln\theta - \varepsilon$ plots. By employing the JMAK model, DRX kinetics model, and grain size model, tailored for BS 080M46 medium carbon steel, parameters were derived from experimental data. Integration of these models into QForm V10.2.1 facilitated hot compression test simulations, offering insights into macroscopic mechanical behavior and microstructure evolution. These simulations revealed several key aspects such as effective strain distribution, DRX volume fraction, and average grain size. Within the FE simulation, the deformation zone exhibited a non-uniform distribution of DRX volume fraction and average grain size due to varying conditions. Notably, elevated temperatures corresponded to increased DRX volume fraction and grain size, whereas a consistent deformation temperature alongside higher strain rates led to reduced DRX volume fraction and grain size. The FE simulation findings closely mirrored the experimental results, with grain sizes obtained from both simulations and experiments under various deformation conditions showing an *AARE* of 7.412% and *R* of 0.991. This close alignment confirms the reliability and efficacy of the grain size model in predicting the grain size of BS 080M46 medium carbon steel during hot working processes.Future research endeavors will focus on translating these insights into practical applications within the automotive manufacturing sector. By leveraging these findings, improvements in process efficiency and product quality can be pursued, thereby enhancing the overall competitiveness and sustainability of manufacturing practices.

Acknowledgments

The authors express their gratitude for the financial support received through the Petchra Pra Jom Klao Ph.D. Research Scholarship (KMUTT-NSTDA) from King Mongkut's University of Technology Thonburi.

References

Alaneme, K.K., Okotete, E.A., 2019. Recrystallization Mechanisms and Microstructure Development In Emerging Metallic Materials: A Review. *Journal of Science: Advanced Materials and Devices,* Volume 4(1), pp. 19–33

Altan, T., 2005. *Cold and Hot Forging: Fundamentals and Applications,* Materials Park, Ohio, ASM International

Anwar, M.S., Melinia, R.K., Pradisti, M.G., Siradj, E.S., 2021. Effect of Prior Austenite Grain-Size on the Annealing Twin Density and Hardness in the Austenitic Stainless Steel. *International Journal of Technology*, Volume 12(6), pp. 1149–1160

Bharath, K., Khanra, A.K., Davidson, M., 2021. Hot Deformation Behavior and Dynamic Recrystallization Constitutive Modeling of Al–Cu–Mg Powder Compacts Processed by Extrusion at Elevated Temperatures*. In:* Proceedings of the Institution of Mechanical Engineers, Part L: Journal of Materials: Design and Applications, Volume 235(3), pp. 581–596

Chen, H., Chen, Z., Liu, J., Wu, Y., Dan, C., Zhong, S., Wang, H., Bréchet, Y., 2021a. Constitutive Modeling of Flow Stress and Work Hardening Behavior While Considering Dynamic Strain Aging. *Materialia,* Volume 18**,** p. 101137

Chen, M.-S., Li, K.-K., Lin, Y.-C., Yuan, W.-Q., 2016. An Improved Kinetics Model to Describe Dynamic Recrystallization Behavior under Inconstant Deformation Conditions. *Journal of Materials Research,* Volume 31(19), pp. 2994–3003

Chen, R., Zhang, S., Liu, X. , Feng, F., 2021b. A Flow Stress Model of 300M Steel for Isothermal Tension. *Materials,* Volume 14(2)**,** p. 252

Chen, X., Liu, B., Zhang, B., Sun, J., Yang, Z., Zhou, X., Huang, T., Yin, D., 2022. Modeling of Dynamic Recrystallization Evolution for Cr8 Alloy Steel and Its Application in FEM. *Materials,* Volume 15(19), p. 6830

Derazkola, H.A., Garcia, E., Murillo-Marrodán, A., Fernandez, A.C., 2022. Review On Modeling and Simulation of Dynamic Recrystallization of Martensitic Stainless Steels During Bulk Hot Deformation. *Journal of Materials Research and Technology*, Volume 18, pp. 2993–3025

Hu, Z., Wang, K., 2020. Evolution of Dynamic Recrystallization in 5CrNiMoV Steel during Hot Forming. *Advances in Materials Science and Engineering,* Volume 2020, p. 4732683

Irani, M., Lim, S., Joun, M., 2019. Experimental and Numerical Study on the Temperature Sensitivity of the Dynamic Recrystallization Activation Energy and Strain Rate Exponent in the JMAK Model. *Journal of Materials Research and Technology*, Volume 8(2), pp. 1616–1627

Jantepa, N., Suranuntchai, S., 2021. Investigation of Hot Deformation Behavior of SNCM8 Alloy Steel. *World Journal of Mechanics,* Volume 11, pp. 17–33

Ji, H., Cai, Z., Pei, W., Huang, X., Lu, Y., 2020. DRX Behavior and Microstructure Evolution of 33Cr23Ni8Mn3N: Experiment and Finite Element Simulation. *Journal of Materials Research and Technology,* Volume 9(3), pp. 4340–4355

Ji, H., Peng, Z., Huang, X., Wang, B., Xiao, W., Wang, S., 2021. Characterization of the Microstructures and Dynamic Recrystallization Behavior of Ti-6Al-4V Titanium Alloy

through Experiments and Simulations. *Journal of Materials Engineering and Performance,* Volume 30(11), pp. 8257–8275

Joun, M.S., Razali, M.K., Chung, S.H., Irani, M., 2022. A Direct Method of Calculating Flow-Related Dynamic Recrystallization Parameters for Generality and Accuracy in Predicting Microstructural Evolution. *Journal of Materials Research and Technology*, Volume 18, pp. 3894–3907

Kooiker, H., Perdahcıoğlu, E.S., Boogaard, A.H.V.d., 2018. A Continuum Model for the Effect of Dynamic Recrystallization on the Stress-Strain Response. *Materials,* Volume 11(5), p. 867

Kozmel, T., Chen, E.Y., Chen, C.C., Tin, S., 2014. Kinetics of Sub-Micron Grain Size Refinement in 9310 Steel. *Metallurgical and Materials Transactions A*, Volume 45(5), pp. 2590–2600

Kurnia, R., Sofyan, B.T., 2017. Effect of Cold Rolling and Annealing Temperature on the Recrystallization and Mechanical Properties of Al-4.7Zn-1.8Mg (wt. %) Alloy Fabricated by Squeeze Casting. *International Journal of Technology,* Volume 8(7), pp. 1329–1335

Lv, Y.-P., Li, S.-J., Zhang, X.-Y., Li, Z.-Y., Zhou, K.-C., 2018. Modeling and Finite Element Analysis for the Dynamic Recrystallization Behavior of Ti-5Al-5Mo-5V-3Cr-1Zr Near β Titanium Alloy During Hot Deformation. *High Temperature Materials and Processes*, Volume 37(5), pp. 445–454

Marques Ivaniski, T., Hatwig, R., Dong, J., Epp, J., Zoch, H., Da Silva Rocha, A., Rocha, S., 2019. An Approach using JMAK Model in Numerical Simulation to Control of Austenitic Grain Size in Hot Forging, *In:* 23rd International Forging Conference - Brazil

Mirzadeh, H., 2015. Constitutive Behaviors of Magnesium and Mg–Zn–Zr Alloy During Hot Deformation. *Materials Chemistry and Physics*, Volume 152, pp. 123–126

Mirzadeh, H., Cabrera, J.M., Najafizadeh, A., Calvillo, P.R., 2012. EBSD Study of a Hot Deformed Austenitic Stainless Steel. *Materials Science and Engineering: A,* Volume 538, pp. 236–245

Mirzadeh, H., Najafizadeh, A., 2010a. Extrapolation of Flow Curves at Hot Working Conditions. *Materials Science and Engineering: A,* Volume 527(7), pp. 1856–1860

Mirzadeh, H., Najafizadeh, A., 2010b. Prediction of the Critical Conditions for Initiation of Dynamic Recrystallization. *Materials & Design,* Volume 31(3), pp. 1174–1179

Mizuguchi, T., Yamashita, M., Terada, D. , Tsuji, N. 2009. Hot Deformation and Dynamic Recrystallization Behaviour of Medium Carbon Steel in Austenite Region. *Steel Research International,* Volume 80(9)**,** pp. 627-631.

Najafizadeh, A., Jonas, J., 2006. Predicting the Critical Stress for Initiation of Dynamic Recrystallization. *ISIJ International*, Volume 46, pp. 1679–1684

Poliak, E., Jonas, J., 2003. Initiation of Dynamic Recrystallization in Constant Strain Rate Hot Deformation. *ISIJ International,* Volume 43(5), pp. 684–691

Quan, G.-Z. 2013. Characterization for Dynamic Recrystallization Kinetics Based on Stress-Strain Curves. *In:* PETER, W. (ed.) *Recent Developments in the Study of Recrystallization.* Rijeka: IntechOpen.

Quan, G.-Z., Shi, R.-J., Zhao, J., Liu, Q., Xiong, W., Qiu, H.-M., 2019. Modeling of Dynamic Recrystallization Volume Fraction Evolution for AlCu4SiMg Alloy and its Application in FEM. Transactions of Nonferrous Metals Society of China, Volume 29(6), pp. 1138–1151

Sanrutsadakorn, A., Uthaisangsuk, V., Suranuntchai, S., 2014. Determination of Initiation of Dynamic Recrystallization in AISI 4340 Steel. *Advanced Materials Research*, Volume 893, pp. 381–386

Shafiei, E., Ebrahimi, R., 2012. A Modified Model to Estimate Single Peak Flow Stress Curves of Ti-IF Steel. *ISIJ International,* Volume 52, pp. 569–573

Stefani, N., Olga, B., Reshetov, A., Blackwell, P., 2016. On the Applicability of JMAK-type Models in Predicting IN718 Microstructural Evolution. *Computer Methods in Materials Science*, Volume 17(1), pp. 59–68

Sun, X., Zhang, M., Wang, Y., Sun, Y., Wang, Y., 2020. Kinetics and Numerical Simulation of Dynamic Recrystallization Behavior of Medium Mn Steel in Hot Working. *Steel Research International,* Volume 91(7), p. 1900675

Tukiat, I.S.T., Yusuf, N.K., Khaireez, H., Al-Alimi, S., Lajis, M.A., Shamsudin, S., Ruhaizat, N.E., 2024. Microstructure and Mechanical Properties of Magnesium ZRE1 (Mg-Zn-Zr) Alloy with Rare Earth Element (Samarium) Addition. *International Journal of Technology*, Volume 15(1), pp. 49–62

Wang, K.L., Fu, M.W., Lu, S.Q., Li, X., 2011. Study of the Dynamic Recrystallization of Ti–6.5Al–3.5Mo–1.5Zr–0.3Si Alloy in β-forging Process via Finite Element Method Modeling and Microstructure Characterization. *Materials & Design,* Volume 32(3), pp. 1283–1291

Wang, W., Zhao, J., Zhai, R., Ma, R., 2016. Arrhenius-Type Constitutive Model and Dynamic Recrystallization Behavior of 20Cr2Ni4A Alloy Carburizing Steel. *Steel Research International,* Volume 88(3), p. 1600196

Wu, Y., Kou, H., Wu, Z., Tang, B., Li, J., 2018. Dynamic Recrystallization and Texture Evolution of Ti-22Al-25Nb Alloy During Plane-Strain Compression. *Journal of Alloys and Compounds,* Volume 749, pp. 844–852

Yang, X., Guo, H., Yao, Z., Yuan, S., 2018. Flow Behavior and Dynamic Recrystallization of BT25y Titanium Alloy During Hot Deformation. *High Temperature Materials and Processes,* Volume 37(2), pp. 181–192

Zhang, K., Wang, K., Lu, S., Liu, M., Zhong, P., Tian, Y., 2022a. Dynamic Recrystallization Behavior and Numerical Simulation of S280 Ultra-High Strength Stainless Steel. *Journal of Materials Research and Technology,* Volume 20, pp. 4419–4431

Zhang, T., Sha, H., Li, L., Lu, S., Gong, H., 2019. Dynamic Recrystallization Kinetics and Microstructure Evolution of 7055 Aluminum Alloy During Hot Compression. *Metallurgical Research & Technology,* Volume 116, p. 605

Zhang, W., Yang, Q., Tan, Y., Ma, M., Xiang, S., Zhao, F., 2020. Simulation and Experimental Study of Dynamical Recrystallization Kinetics of TB8 Titanium Alloys. *Materials,* Volume 13(19), p. 4429

Zhang, Y.Q., Quan, G.Z., Lei, S., Zhao, J., Xiong, W., 2022b. Description of Dynamic Recrystallization Behaviors and Grain Evolution Mechanisms during the Hot Forming Process for SAE 5137H Steel. *Materials,* Volume 15(16), p. 5593

Zheng, Y., Liu, D., Yang, Y., Zhang, Z., Li, X. , Zhang, R. 2018. Microstructure Evolution of Ti-6Al-4V with Periodic Thermal Parameters During Axial Closed Die Rolling Process. *Journal of Alloys and Compounds,* Volume 735**,** pp. 996-1009

Zou, X., Yan, Z., Zou, K., Liu, W., Song, L., Li, S., Cha, L., 2022. Grain Refinement by Dynamic Recrystallization during Laser Direct Energy Deposition of 316L Stainless Steel Under Thermal Cycles. *Journal of Manufacturing Processes*, Volume 76, pp. 646–655